ADVANCED MATERIALS INTERFACES
Open Access
www.advmatinterfaces.de

Check for updates

Correlated Intrinsic Electrical and Chemical Properties of Epitaxial WS_2 via Combined C-AFM and ToF-SIMS Characterization

Valentina Spampinato, Yuanyuan Shi, Jill Serron, Albert Minj, Benjamin Groven, Thomas Hantschel, Paul van der Heide, and Alexis Franquet*

Atomically thin, 2D semiconductors, such as transition metal dichalcogenides, complement silicon in ultra-scaled nano-electronic devices. However, the semiconductor and its interfaces become increasingly more difficult to characterize chemically and electrically. Conventional methodologies, including scanning probe microscopies, fail to capture insight into the chemical and electronic nature of the semiconductor, albeit vital to understand its impact on the semiconductor performance. Therefore, this work presents a unique and universal in situ approach combining time-of-flight secondary ion mass spectrometry and atomic force microscopy to map chemical differences between regions of different electrical conductivity in epitaxially deposited tungsten disulfide (WS_2) on sapphire substrates. Surprisingly, WS_2 regions of lower electrical conductivity possess a larger amount of sulfur compared to regions with higher conductivity, for which oxygen is also detected. Such difference in chemical composition likely roots from the non-homogeneously terminated sapphire starting surface, altering the WS_2 nucleation behavior and associated defect formation between neighboring sapphire terraces. These resulting sapphire terrace-dependent doping effects in the WS_2 hamper its electrical conductivity. Thus, accurate chemical assignment at a sub-micrometer lateral resolution of atomically thin 2D semiconductors is vital to achieve a more detailed understanding on how the growth behavior affects the electrical properties.

1. Introduction

Two-dimensional (2D) transition metal dichalcogenides (TMDs) with general formula MX_2 (with M being a transition metal and X a chalcogen) promise to be the next-generation semiconductor platform[1–6] providing the sought-after complementary metal oxide semiconductor technology downscaling. In particular, molybdenum and tungsten disulfide (MoS_2, WS_2) receive considerable attention in both scientific and industrial research communities in view of their unique chemical, thermal, electrical, and optoelectrical properties.[7]

To enable such a 2D semiconductor platform, several manufacturable thin film deposition techniques have been investigated for the deposition of highly crystalline and functional TMD monolayers (MLs) on large-area substrates.[8] Metal-organic chemical vapor deposition (MOCVD) of TMD monolayers from a metal-organic (e.g., tungsten hexacarbonyl, $W(CO)_6$) and dihydrogen sulfide (H_2S) precursors, is one of the most technologically viable deposition approaches on single crystalline templates, such as sapphire. In this deposition approach, the TMD crystals develop a preferred in- and out-of-plane crystallographic orientation by exploiting sapphire's epitaxial seeding capability.[9–14] As such, electrically detrimental crystal grain boundaries can be eliminated from the TMD monolayer, resulting in state-of-the-art device performance.

Interestingly, due to their atomically thin nature, the TMD monolayer properties and device performance can be heavily affected by the nature of the underlying starting surface and the environment.[15–17] For example, and with respect to the latter, oxygen and humidity from the ambient or contaminants, play a crucial role in determining the device performance and lifetime, as well as the optical and electronic properties of 2D TMDs.[18–23]

In our previous work,[24] MoS_2 monolayers from MOCVD on c-plane single-crystalline sapphire exhibit an inhomogeneous distribution in electrical conductivity directly imposed by the non-uniform surface topography of the underlying sapphire terraces, as elucidated by conductive atomic force microscopy

V. Spampinato, J. Serron, A. Minj, T. Hantschel, P. van der Heide, A. Franquet
Materials and Components Analysis (MCA)
IMEC
Kapeldreef 75, Leuven 3001, Belgium
E-mail: valentina.spampinato@imec.be
Y. Shi
School of Microelectronics
University of Science and Technology of China
No.96, JinZhai Road Baohe District, Hefei, Anhui 230026, P. R. China
B. Groven
Materials-Interfaces, Deposition-Analysis (MIDA)
IMEC
Kapeldreef 75, Leuven 3001, Belgium
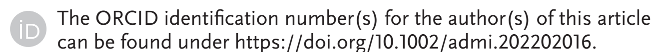
The ORCID identification number(s) for the author(s) of this article can be found under https://doi.org/10.1002/admi.202202016.

© 2023 The Authors. Advanced Materials Interfaces published by Wiley-VCH GmbH. This is an open access article under the terms of the Creative Commons Attribution License, which permits use, distribution and reproduction in any medium, provided the original work is properly cited.

DOI: 10.1002/admi.202202016

 © 2023 The Authors. Advanced Materials Interfaces published by Wiley-VCH GmbH

21967350, 2023, 7, Downloaded from https://onlinelibrary.wiley.com/doi/10.1002/admi.202202016 by EVIDENCE AID - BELGIUM, Wiley Online Library on [08/06/2023]. See the Terms and Conditions (https://onlinelibrary.wiley.com/terms-and-conditions) on Wiley Online Library for rules of use; OA articles are governed by the applicable Creative Commons License

(C-AFM). The differences in sapphire surface topography imply variations in its surface termination and/or surface structure per sapphire terrace. In turn, this can either affect the MoS_2 nucleation behavior per sapphire terrace introducing intragrain defects in the MoS_2 monolayer, or alter the MoS_2 interface defectivity. We proposed these sapphire surface anomalies result in terrace-dependent local doping effects in the MoS_2 monolayer that hamper the electrical conductivity of MoS_2.

However, conventional characterization methodologies fail to capture insight into the chemical and electronic nature of the TMD interfaces, albeit vital to unravel how the MOCVD growth behavior and the sapphire starting surface affect the TMD electrical performance. Such insight is instrumental to leverage TMDs from the laboratory scale to industrially relevant applications. Today, a systematic study and comprehensive interpretation of the electronic response of TMDs when impacted by defects, airborne molecules, impurities, and substrate surface termination is still lacking.[25–27]

This general lack of insight highlights the need for a characterization methodology where electrical, structural, and chemical characterization is combined. Undoubtedly, this requires a chemical characterization technique that can provide sufficient lateral resolution to discriminate the surface termination and composition between high and low conductive regions in the TMD layer, together with high sensitivity.

Time-of-flight secondary ion mass spectrometry (ToF-SIMS) is an extremely surface-sensitive technique, which provides both elemental and molecular information on surfaces and thin films. This technique is currently well-established, among the others, for chemical mapping of different organic and inorganic materials and nanolayered systems with a lateral resolution down to 100 nm.[28] Certainly, ToF-SIMS has been already successfully applied to locate the metal and the chalcogen in flakes of MX_2 layers with large (tens of microns) domains.[29,30] When ToF-SIMS is coupled with an in situ AFM module, both electrical and chemical information of the TMD layer can be revealed by performing consecutive C-AFM and ToF-SIMS analysis on the very same position.

This methodology can be regarded as a universal characterization approach for any type of TMDs. However, some limitations could be encountered when dealing with very small features and very thin layers. For this reason, in this proposed characterization methodology, WS_2 is chosen over MoS_2 used in our previous work, as the observed regions in the WS_2 of different electrical conductivity appear significantly larger in lateral dimensions facilitating the ToF-SIMS analysis. Moreover, a ≈2.5 ML system was preferred to the monolayer one to allow for a higher count rate during ToF-SIMS chemical mapping.

From the combined ToF-SIMS and AFM inspection, WS_2 regions of lower electrical conductivity are mainly characterized by sulfur, while regions with higher conductivity appear to also contain oxygen. Such difference in chemical composition possibly originates from the non-homogeneously terminated sapphire starting surface since, during the WS_2 MOCVD process, sapphire could reconstruct conceivably introducing defect-free and defect-containing WS_2 layers.

2. Results and Discussion

2.1. Non-homogeneous Electrical Conductivity and Surface Potential of WS_2 MOCVD on Sapphire

In this first section, the (offline) C-AFM results obtained on a ≈2.5 ML WS_2 epitaxially deposited on sapphire, as detailed in the Experimental Section, are discussed.

In C-AFM, information on the surface roughness and conductivity at the nanoscale is collected simultaneously by scanning a metallic AFM tip in contact mode over the sample surface, whilst applying a DC bias voltage.

Figure 1a,b shows the C-AFM data of the ≈2.5 ML WS_2, where a low conductive area in the current map (Figure 1b) perfectly matches an area in the topography (Figure 1a), following the shape of an underlying sapphire terrace, as indicated by the dashed green outline. Here, the conductivity drops down to the noise level of the current amplifier. It is worth mentioning that WS_2 islands located on different sapphire terraces

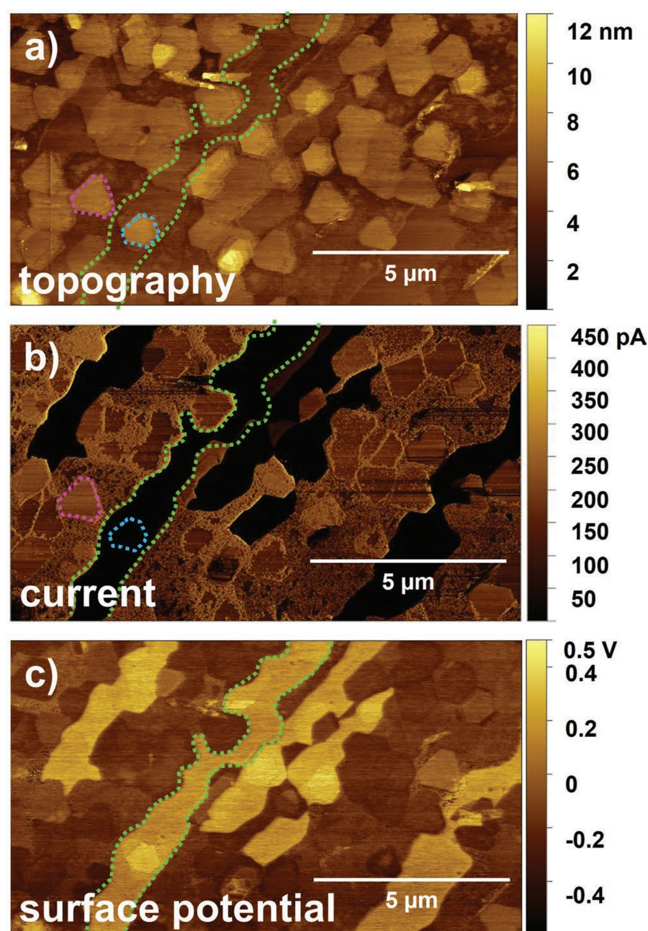

Figure 1. Topography (a), current (b) and surface potential (c) map of a ≈2.5 ML WS_2 on on-axis cut sapphire. The area indicated by the green dashed line in (a) follows the shape of an underlying sapphire terrace that perfectly matches a region with lower conductivity (b) and higher surface potential (c). WS_2 islands located on different sapphire terraces and exhibiting different conductivity (a,b) are marked in blue (lower conductivity) and pink (higher conductivity).

© 2023 The Authors. Advanced Materials Interfaces published by Wiley-VCH GmbH

clearly display quite dissimilar conductivity, as shown in Figure 1a,b by the blue (lower conductivity) and pink (higher conductivity) dashed outlines. This difference in conductivity, therefore, seems to suggest a correlation with terrace specificity.

Moreover, these WS_2 regions with comparatively lower conductivity demonstrate a higher surface potential in frequency modulated Kelvin probe force microscopy (FM-KPFM), as indicated by the dashed green outline in Figure 1c. Considering, that the AC bias is applied to the sample, higher surface potential values imply a higher work function in the tool setup used during this measurement. In a recent work (manuscript in preparation), scanning tunneling spectroscopy on a similar WS_2 layer grown on sapphire, allowed to deduce that the WS_2 layer is an n-type semiconductor. In that case, electrons are the majority carriers meaning that the Fermi level is closer to the conduction band, thus a smaller work function is achieved in comparison to the intrinsic material properties. Nevertheless, a significant increase in surface potential of ≈0.5 V, hence an increased work function by ≈0.5 eV, is exhibited for the poorly conducting terraces. For the n-type WS_2, this conveys that the Fermi level position has shifted further from the conduction band, resulting in a dramatic decrease in the free electrons. Here, the higher work function for the low conductive regions is likely due to the presence of negatively charged defects, but their precise location in the 2D layer remains unknown. One may consider that the conductivity in highly conductive regions with S-vacancies should also decrease with their passivation by oxygen atoms as S-vacancies have been reported to be donors, thus leading to a higher work function. However, we must emphasize that the n-type conductivity of the 2D layers is not only contributed by S-vacancies, but also by other factors, which are not affected by O-passivation. For example, the electron transfer from the substrate to the 2D layer and the substrate-induced strain are additional sources of n-type carriers. Computational studies of the band structure and the density of states of TMD layers and the Al_2O_3 interface,[31] strongly support the electron transfer from the substrate to the 2D layer. Furthermore, the strain induced by the Al_2O_3 substrate on the 2D layer was proven to lead to n-type doping.[32]

These non-homogeneous distributions in conductivity and surface potential suggest that a chemical difference exists between the different WS_2 regions on sapphire. However, the C-AFM and KPFM alone are not sufficient to explain the correlation between chemical and electrical properties, thus ToF-SIMS analysis was conducted on the same layers in an attempt to ultimately obtain a clear correlation.

2.2. Choosing the Preferred ToF-SIMS Analysis Mode: Trade-Off Between Lateral Resolution and Chemical Assignment

ToF-SIMS data acquisition can be carried out using the analysis beam in different acquisition modes. Each mode is better suited for a specific purpose, such as best count rate, best mass resolution, or best lateral resolution. Please note that mass resolution, lateral resolution, and count rate cannot be optimized simultaneously during ToF-SIMS measurements.[33] In this study, we decided to compare four different ToF-SIMS acquisition modes to assess whether a high mass resolution was needed to discriminate the ions of interest and which mode could provide sufficient lateral resolution together with an optimal ionic count rate.

For this purpose, the Spectrometry and Fast Imaging (FI) modes were compared, together with the FI mode coupled with delayed extraction and Burst mode. The Spectrometry mode exhibits high mass resolution and count rate, whereas the FI mode possesses a high lateral resolution but only at unit mass resolution. By coupling the FI mode with delayed extraction, it displays improved mass resolution compared to FI. Last, the Burst mode presents rather a compromise between the two above-mentioned modes.

The Spectrometry mode was only used to unambiguously define the mass peaks and their assignments, since the mass resolution (beam spot size ≈3 μm) is not sufficient to resolve the sample's distinct features. Moreover, to avoid collecting ions mainly from the substrate (due to the very low thickness of the WS_2 layer), only the very first scans of the acquisition were considered, much before the rising of the substrate signal, that is Al-related ions.

As explained in the Experimental Section, the sample substrate is sapphire (Al_2O_3) and the 2D material layer is WS_2. Therefore, we had to assess whether, for example, O_2^-, related to the sapphire substrate, was separated from S^-, related to the WS_2 layer, since the two have the same unit mass. Moreover, it is important to evaluate whether the chosen acquisition mode allows for a sufficient count rate, since the WS_2 layer is quite thin and it will be consumed rapidly during the acquisition.

If we consider the integrated area of the mass peaks cantered at m/z 32, the FI mode allows for the highest count rate (**Figure 2**a). This is also confirmed by the total ion images reported in Figure 2b (i.e., intensity bars). Please keep in mind that in this study the Spectrometry mode is only reported as a reference for the peaks' assignment but cannot be used due to the low lateral resolution (see Figure 2b, top left). When considering the Spectrometry mode, O_2^- seems to be barely present in the first acquisition scans (see Figure 2a), and, therefore, the FI mode can be clearly used in negative polarity for this kind of samples.

Moreover, when comparing the lateral resolution attainable on WS_2 with the different acquisition modes, the different sapphire terraces are most clearly discriminated in the field of view of the two FI modes, as indicated by the darker and brighter regions (Figure 2b). In contrast, the sapphire terrace features appear blurry in Burst mode and completely indistinguishable in Spectrometry mode, as expected. Therefore, the FI mode provides the best compromise between lateral resolution and chemical information, and, for these reasons, it was chosen to carry out the experiments on the TMD layers.

2.3. Combined ToF-SIMS and AFM: Correlating Chemical and Electrical Properties

In order to perform a correlative study on the ≈2.5 ML WS_2 already characterized via offline AFM, in situ C-AFM was performed on the combined ToF-SIMS/in situ-AFM tool.

The WS_2 layer was first scanned in contact mode with a full diamond conductive tip to acquire the current map of the

© 2023 The Authors. Advanced Materials Interfaces published by Wiley-VCH GmbH

21967350, 2023, 7, Downloaded from https://onlinelibrary.wiley.com/doi/10.1002/admi.202202016 by EVIDENCE AID - BELGIUM, Wiley Online Library on [08/06/2023]. See the Terms and Conditions (https://onlinelibrary.wiley.com/terms-and-conditions) on Wiley Online Library for rules of use; OA articles are governed by the applicable Creative Commons License

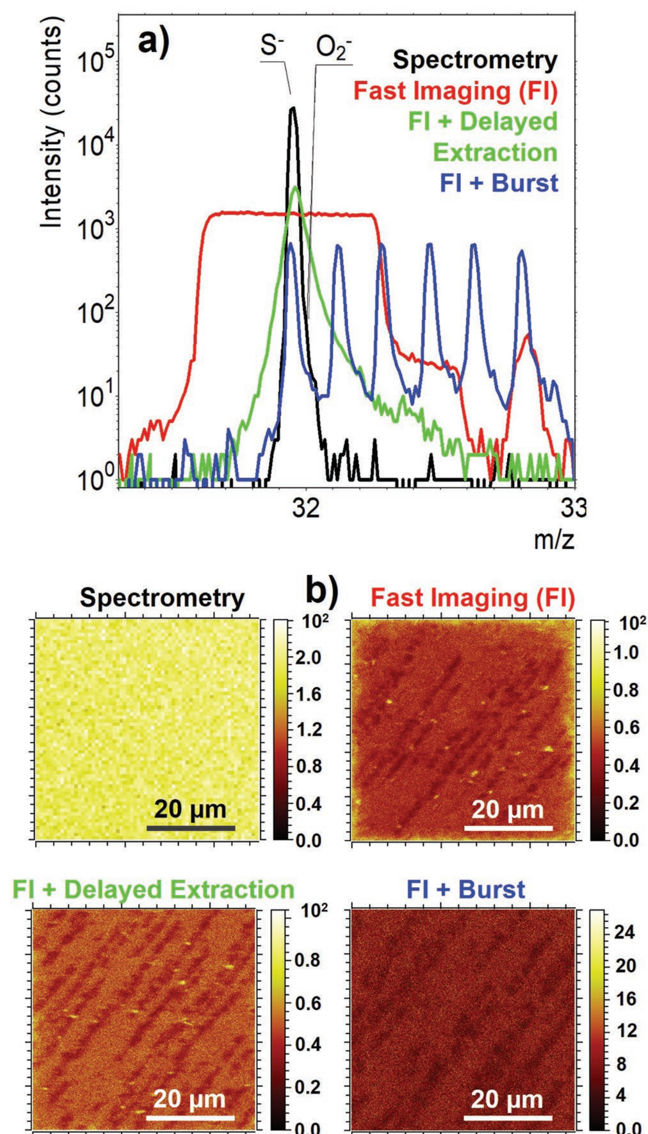

Figure 2. a) ToF-SIMS spectra overlay for m/z 32 for four different acquisition modes: Spectrometry (black), Fast Imaging (FI, red), FI coupled with delayed extraction (green), and FI coupled with Burst mode (blue). b) ToF-SIMS total ion maps for the above-mentioned acquisition modes indicating the presence of different terraces (brighter and darker regions, not discernible in the Spectrometry mode).

area, as reported in **Figure 3**a. From the current map, areas with lower conductivity can be observed (darker areas) characterized by an elongated shape (i.e., sapphire terraces), as previously observed in the offline AFM experiments described in Section 1.1. In the bright regions, the current registered was in the range of 1.6–1.9 nA, while in the dark areas in the range of 0.4–0.8 nA.

After the C-AFM acquisition, a ToF-SIMS chemical map was collected in the same area (Figure 3b), thanks to the use of the combined ToF-SIMS/in situ-AFM tool. From the comparison of the current and total ion image maps in Figure 3, we can assess that the low conductive areas are correlated to the dark areas in the total ion image.

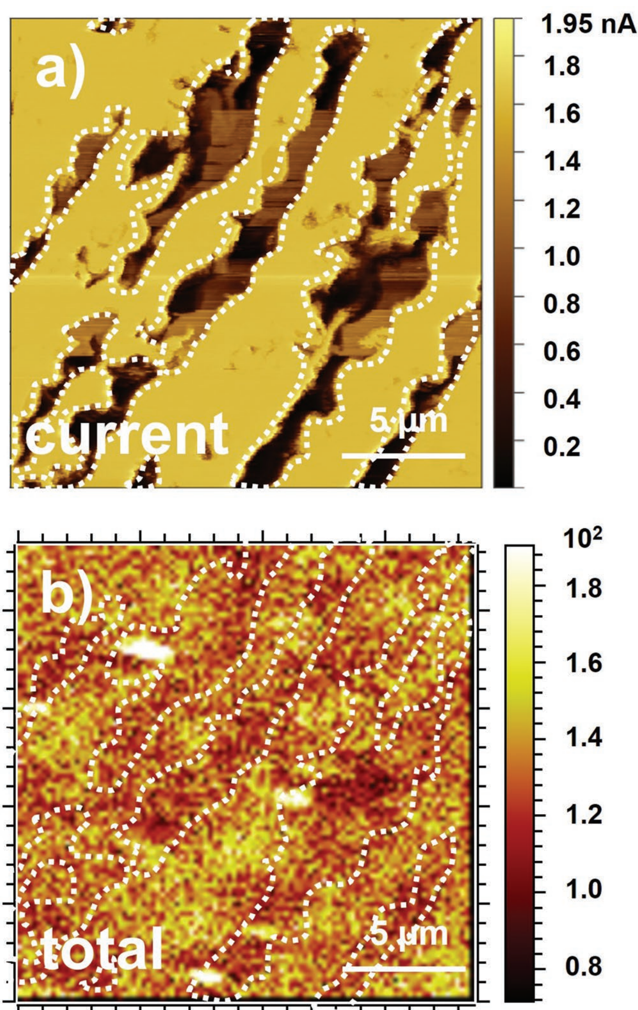

Figure 3. a) Current map of ≈2.5 ML WS_2 acquired with in situ C-AFM. b) ToF-SIMS total ion map from the same area as (a).

Unfortunately, we noticed that the C-AFM scan did somehow damage the WS_2 surface, as it can be observed in **Figure 4** where a ToF-SIMS image larger than the C-AFM scanned area was recorded. Here, the area scanned in contact mode shows a contrast with the pristine area, suggesting that the layer was probably partially removed and/or damaged during the scan. However, even when using a Pt/Ir-coated probe, a much softer probe than the diamond one used in this work, some damage was still detected on the sample (data not shown). Thus, this behavior could be as well related to some tip-induced charging effect, which would deteriorate the ToF-SIMS ion image quality.

For this reason, we decided to collect the current information on some areas of the sample and perform the ToF-SIMS experiments on different (fresh) areas. In fact, from the first experiment reported in Figure 3, we have already established that dark areas in the current maps (low current) correspond to dark areas in the ToF-SIMS total ion images. We can, hence, refer to the total ion image as a representation of the current map and further collect information about the specific ions detected in the two different areas (bright vs dark).

© 2023 The Authors. Advanced Materials Interfaces published by Wiley-VCH GmbH

21967350, 2023, 7, Downloaded from https://onlinelibrary.wiley.com/doi/10.1002/admi.202202016 by EVIDENCE AID - BELGIUM, Wiley Online Library on [08/06/2023]. See the Terms and Conditions (https://onlinelibrary.wiley.com/terms-and-conditions) on Wiley Online Library for rules of use; OA articles are governed by the applicable Creative Commons License

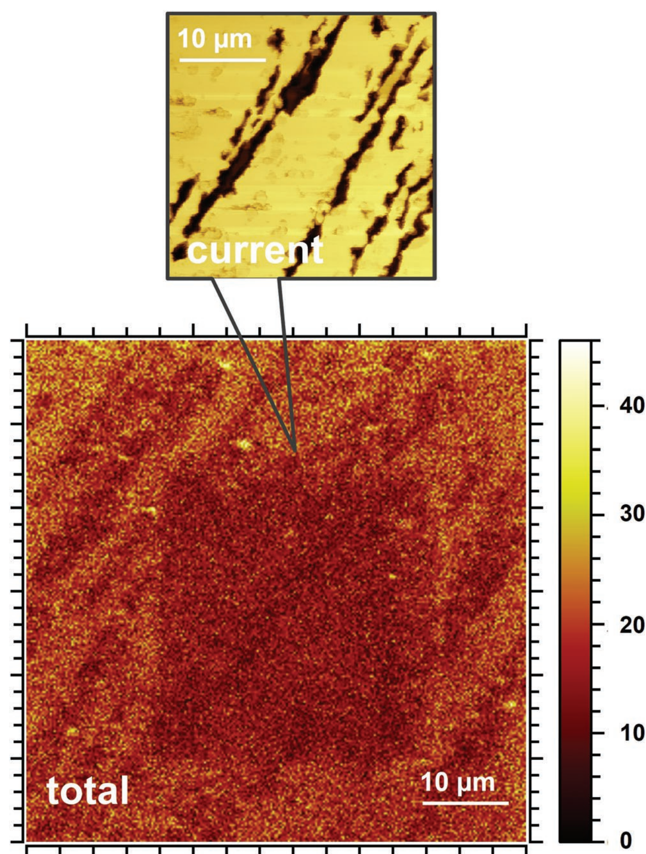

Figure 4. ToF-SIMS total ion map of ≈2.5 ML WS_2 (bottom) cantered on an area previously scanned with in situ C-AFM (top).

2.4. Identifying the Chemical Contrast on WS_2 layers via ToF-SIMS Chemical Maps Study

From the ToF-SIMS experiments performed on the ≈2.5 ML WS_2, seven types of ions can unambiguously be defined and assigned to WS_2 and sapphire by comparing the Spectrometry mode to the isotopic pattern distribution calculation. These ions include O^-, S^-, S_2^-, SO_3^- and WS_3^- in negative polarity and W^+ and WS^+ in positive polarity. However, since the positive detection mode did not provide additional information to the negative one, we focus on the negative ions in the remainder of the article.

In addition, we specifically explored ions originating from either the sapphire terraces and its surface terminations (i.e., Al-S, Al-O_x, Al-Al), from defects in the WS_2 film (i.e., W_2, WO_x) and from the interface between WS_2 and sapphire (i.e., Al-W). Unfortunately, none of these ions could be detected or assigned, either due to their intensity falling below the detection limit or due to ambiguity in their assignment, such is the case for WO_x.

Therefore, only the chemical maps are reported for the above-mentioned five negative ions that were clearly detected and assigned. They are represented as intensities collected in FI mode and normalized to the total ion intensity (**Figure 5**). This normalization procedure was chosen to compensate for possible artifacts related to the different ions' ionization yield.[34]

As previously mentioned, dark regions of low electrical conductivity in the current map also correspond to dark regions in the ToF-SIMS total ions image. From the chemical maps of the individual ions (Figure 5), high current regions appearing bright in the current map emerge as oxygen-containing (i.e., O^-, SO_3^-) areas, while low current regions appear to be strongly characterized by sulfur (i.e., S^-, S_2^-, WS_3^-) and contain more Al (Al^+) and W (W^+) (data not shown). Moreover, the contours

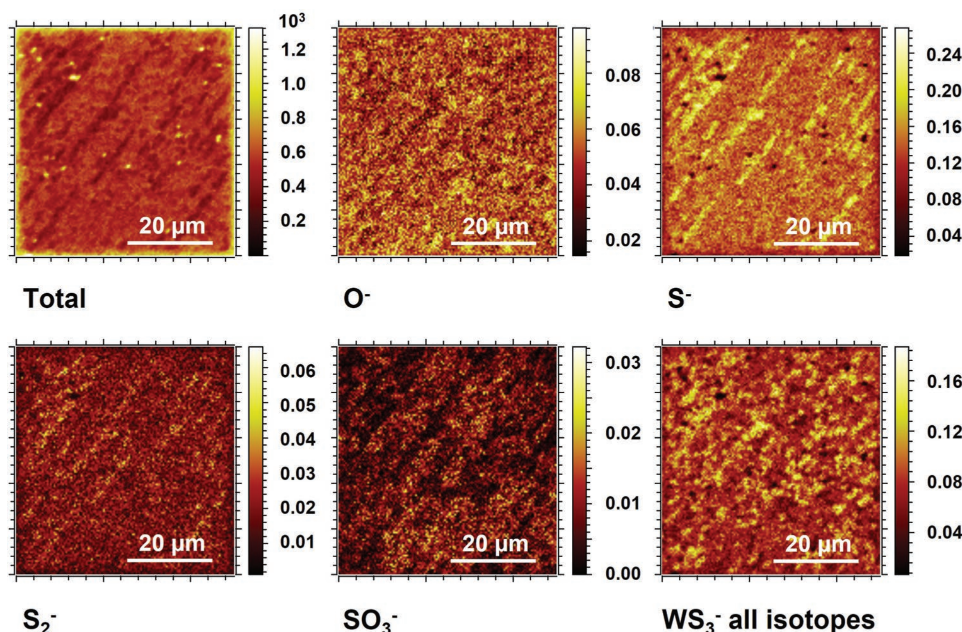

Figure 5. ToF-SIMS chemical maps (FI mode) of different ions of interest: Total ions, O^-, S^-, S_2^-, SO_3^- and all isotopes of WS_3^-.

© 2023 The Authors. Advanced Materials Interfaces published by Wiley-VCH GmbH

21967350, 2023, 7, Downloaded from https://onlinelibrary.wiley.com/doi/10.1002/admi.202202016 by EVIDENCE AID - BELGIUM, Wiley Online Library on [08/06/2023]. See the Terms and Conditions (https://onlinelibrary.wiley.com/terms-and-conditions) on Wiley Online Library for rules of use; OA articles are governed by the applicable Creative Commons License

ADVANCED MATERIALS INTERFACES
Open Access
www.advmatinterfaces.de

of the sulfur-rich regions in the chemical maps correspond to the height contours in the topography map collected at the same location, hinting yet again that the observed chemical and electrical differences are strongly correlated to the underlying sapphire surface termination and structure.

The observed inhomogeneous distribution and correlation between the current and chemical maps do not originate from local variations in WS_2 layer thickness. If the number of WS_2 layers locally varies or WS_2 is even absent, revealing the non-conductive sapphire substrate, the ToF-SIMS chemical maps should display the opposite trend. That is, low-conductive regions are characterized by sapphire-related elements such as aluminum and oxygen, whereas the high-conductive regions pertain to WS_2-related elements such as tungsten and sulfur. Our findings from the ToF-SIMS measurements are in clear contrast with this theory, excluding a correlation with the absence of the WS_2 layer and the direct detection of the sapphire substrate. Indeed, also the AFM topographical maps confirmed the presence of the WS_2 layer all over the sapphire surface (see Figure 1a).

A more plausible hypothesis relates to an inhomogeneous sapphire surface termination, as schematically depicted in **Figure 6**a. As reported in our previous study,[24] the sapphire terminations influence the MX_2 nucleation, occurring preferably on some terraces rather than others. With time, the MX_2 nuclei grow laterally and coalesce to form the monolayer, fully covering the whole sapphire surface. However, the influence of the sapphire surface termination on the nucleation can lead to different defects in the first monolayer, such as intra-grain defects, etc.

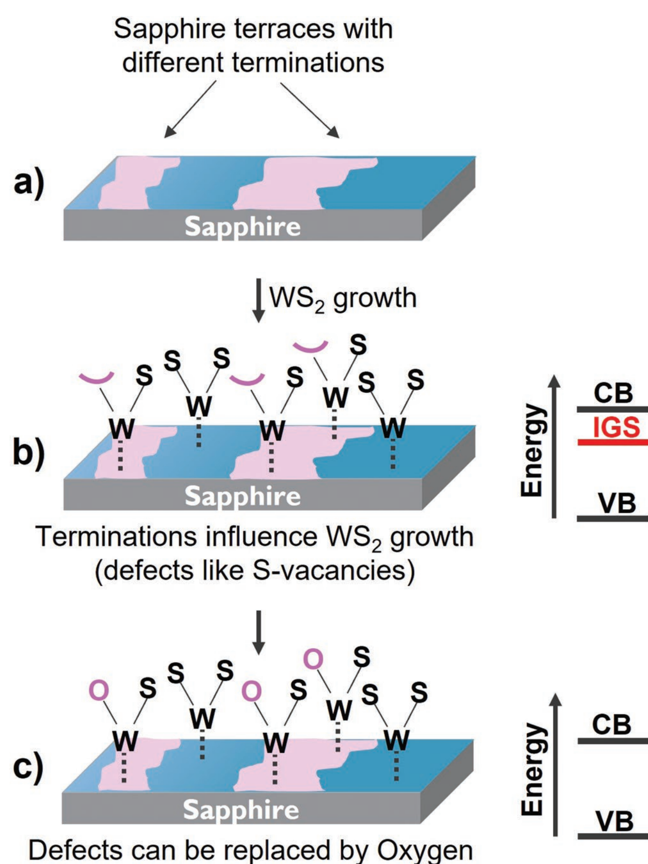

Figure 6. a) Schematic representation of a sapphire substrate with different surface terminations (blue vs pink areas). b) Possible chalcogenide vacancy formation triggered by the different surface terminations during WS_2 nucleation and related energy band distribution. c) Possible oxygen substitution at the previously formed vacancy sites and related energy band distribution. CB stays for the conduction band, VB for the valence band, and IGS for the induced gap state.

For instance, it is well known that dichalcogenides have the tendency to develop defects in the form of chalcogenide vacancy,[35] as depicted in Figure 6b. When these vacancies form, the band gap changes creating a trap band between the valence and the conduction bands, as schematically depicted in the right-hand side of Figure 6b. This can easily trap electrons and therefore drastically reduce the conductivity. It was demonstrated that it is possible to regenerate a quasi-pristine status with the substitution of the vacancy with different atoms.[36–39] One of the most suitable elements to do so is oxygen, because it is iso-electronic to sulfur (see schematics in Figure 6c). This substitution can happen via interaction with the air, absorption of water, annealing, etc.

If this is the case, we could possibly detect areas where the substitution successfully occurred and areas where the sulfur vacancies are still present. This would define two regions with strongly different conductivity, as we observed in the C-AFM maps. This would as well explain why the low conductive regions appear to be sulfur-rich, while the highly conductive regions are characterized by oxygen. In fact, ToF-SIMS detects S^- everywhere in the analyzed area, but with different intensities. Since ToF-SIMS is not sensitive to "vacancies", what is actually observed in the high conductive areas is the sulfur intensity attenuated by the oxygen presence. This is strongly supported by the detection of the SO_3^- cluster, which is only present in the highly conductive regions and complementary to the sulfur-rich areas (see Figure 5). Based on the concept of the Self-Focusing SIMS,[40] such a cluster cannot be formed if sulfur and oxygen (i.e., the cluster's constituents) are not present simultaneously and in close proximity in the same physical point on the analyzed area. This cluster clearly demonstrates the passivation on the sulfur-vacancy sites and that this did not happen homogeneously in the layer, but it was possibly related to the above-mentioned sapphire surface terminations, which lead to the different presence of defects in the WS_2 layer. On the other hand, the probability of forming an S_x or WS_x cluster is more pronounced in the areas where oxygen is not present, as demonstrated by the S_2^- and WS_3^- chemical maps in Figure 5. The regions in which these sulfur-based clusters are more noticeable are indeed the low conductive regions detected by C-AFM.

3. Conclusion

In this study, a combined ToF-SIMS/in situ-AFM instrument was used to correlate the intrinsic electrical and chemical properties of epitaxial WS_2 deposited on sapphire. From the C-AFM experiments, the sample was found to display a non-homogeneous current distribution, showcasing a drop in conductivity for certain WS_2 terraces. Besides that, KPFM data revealed that higher surface potential values were obtained for these regions,

© 2023 The Authors. Advanced Materials Interfaces published by Wiley-VCH GmbH
21967350, 2023, 7, Downloaded from https://onlinelibrary.wiley.com/doi/10.1002/admi.202202016 by EVIDENCE AID - BELGIUM, Wiley Online Library on [08/06/2023]. See the Terms and Conditions (https://onlinelibrary.wiley.com/terms-and-conditions) on Wiley Online Library for rules of use; OA articles are governed by the applicable Creative Commons License

implying that the material had a decreased n-doping. The ToF-SIMS chemical maps provided clear information about the chemical elements' distribution in the two (lower vs higher) conductive regions. The poorly conductive areas were found to be sulfur-rich, while the highly conductive ones were correlated with oxygen-containing regions. A difference in the sapphire terminations, and the correlated nucleation process during WS_2 growth, was postulated to be possibly responsible for such different conductive regions. This methodology is here presented as a universal approach for correlative characterization of any TMD for which differences in conductivity are observed and need to be correlated with chemical changes in the layer, starting surface, terminations, etc. Some limitations could be encountered for samples with very small domains (i.e., below the ToF-SIMS lateral resolution) and very thin layers, since this will affect the ions' intensity deteriorating the detection limit. However, for all the cases in which these preconditions are met, the proposed methodology can be definitively considered as a brilliant and unique approach to characterize TMDs of different kinds.

The results obtained in this study, clearly demonstrate the need for combined electrical and chemical characterization to fully understand the behavior of TMDs and how defects and/or impurities can affect their performance.

4. Experimental Section

MOCVD of WS_2 on Sapphire Substrate: The ≈2.5 ML WS_2 was grown on a 2-inch c-plane (0001) single-crystalline on-axis cut sapphire, α-Al_2O_3 (from the Roditi International Corporation) by MOCVD (Epsilon3200, ASM). Prior to the growth of WS_2, the sapphire wafers were thermally annealed in an O_2 atmosphere for 1 h at 1175 °C to remove residues or contaminants on the sapphire surface. The previous study[41] shows that this pre-epi sapphire treatment could result in a reconstructed ($\sqrt{31} \times \sqrt{31}$) R9 Al-terminated sapphire surface. The details regarding the sapphire pre-epi treatment and WS_2 deposition were reported in the previous work.[24] The sapphire substrate was first heated to 1000 °C under a high-purity N_2 environment after introducing it into the MOCVD reactor, then 1000 sccm H_2S and 1000 sccm Ar: $W(CO)_6$ gas precursors were delivered to the reactor. The H_2S was carried by 15 slm N_2. The flow rate of $W(CO)_6$ was 0.102 sccm, which was carried by Ar. High-purity H_2S, N_2, and Ar gas were provided through compressed gas cylinders. The $W(CO)_6$ was vaporized from the solid precursor in a metallic canister (from Air Liquide) at ≈31 °C under ≈800 mbar. During the growth, the temperature was kept at 1000 °C and the total pressure was constant at 150 Torr for 360 min, which results in ≈2.5 ML WS_2. The thickness was checked through Rutherford Backscattering Spectrometry. After the deposition, an H_2S post-deposition annealing process was introduced to further improve the WS_2 crystallinity.

ToF-SIMS Analysis: The tool used in this study is a hybrid instrument, which combines in the same UHV analysis chamber a ToF-SIMS unit with an AFM module (ToF-SIMS NCS, ION-TOF GmbH, Münster, Germany). More details about this combined tool can be found in the previous work.[42] The ToF-SIMS analysis was performed using a Bismuth liquid metal cluster ion gun (LMIG), using Bi_3^+ species, on square areas (between 20 and 60 μm^2) with a resolution of 1024 × 1024 pixels. Different acquisition modes were compared in this study. The Spectrometry mode was used for its high mass resolution ($m/\Delta m$ >7000 at m/z 29) to define certain peaks assignment. The FI mode was used for its high lateral resolution (beam spot size <150 nm) to obtain chemical maps of the conductive domains. FI mode coupled with delayed extraction (beam spot size <150 nm) and Burst mode (beam spot size <300 nm) were used as a compromise between good mass and lateral resolution, since the FI mode alone allowed only unit mass resolution. The different modes used in this study are described in detail in Section 1.2.

C-AFM Analysis: The in situ C-AFM analysis was performed in the combined ToF-SIMS/in situ-AFM tool previously described[34] in contact mode using an in-house fabricated heavily boron-doped diamond tip[43] attached to a nickel cantilever with a spring constant of ≈11 N m^{-1}. A bias of +5 V was applied to the cantilever during the C-AFM map acquisition on scan areas of (usually) 20 × 20 μm^2. Typically, a set point of 550 nN and a scan rate of 10 µm s^{-1} were used. The analysis was performed under UHV conditions, that is, ≈10^{-9} mbar.

The offline C-AFM experiment was conducted on a Dimension Icon-PT system from Bruker placed in an Ar-filled glovebox. The experiment was performed at a 0.3 Hz scan rate, a setpoint of ≈40–50 nN was used and a DC bias of +0.5 V was applied to the sample. For these measurements, a Pt/Ir coated probe, PPP-EFM (NanoAndMore), with a spring constant of ≈2.5 N m^{-1} and a natural frequency of ≈75 kHz was used. To ensure electrical connection to the sample, a fast-drying silver paste was directly applied onto the WS_2 layer as a back contact.

FM-KPFM Analysis: FM-KPFM was carried out on a Dimension Icon-PT system from Bruker placed in an Ar-filled glovebox. During the measurement, an AC bias of +2 V was applied to the sample. A Pt/Ir coated probe, PPP-NCSTPt (NanoAndMore), with a spring constant of ≈7.4 N m^{-1} and a natural frequency of ≈160 kHz was used. To ensure an electrical connection to the sample, a fast-drying silver paste was used as a back contact.

Acknowledgements

The authors would like to acknowledge Pierre Morin for the valuable inputs and suggestions provided regarding the MX_2 growth process.

Conflict of Interest

The authors declare no conflict of interest.

Data Availability Statement

Research data are not shared.

Keywords

2D materials, conductive atomic force microscopy (C-AFM), correlative microscopy, Kelvin probe force microscopy (KPFM), time-of-flight secondary ion mass spectrometry (ToF-SIMS)

Received: September 12, 2022
Revised: December 8, 2022
Published online: January 3, 2023

[1] S. B. Desai, S. R. Madhvapathy, A. B. Sachid, J. P. Llinas, Q. Wang, G. H. Ahn, G. Pitner, M. J. Kim, J. Bokor, C. Hu, H.-S. P. Wong, A. Javey, *Science* **2016**, *354*, 99.
[2] Y.-Q. Bie, G. Grosso, M. Heuck, M. M. Furchi, Y. Cao, J. Zheng, D. Bunandar, E. Navarro-Moratalla, L. Zhou, D. K. Efetov, T. Taniguchi, K. Watanabe, J. Kong, D. Englund, P. Jarillo-Herrero, *Nat. Nanotechnol.* **2017**, *12*, 1124.
[3] Y. Shi, X. Liang, B. Yuan, V. Chen, H. Li, F. Hui, Z. Yu, F. Yuan, E. Pop, H. S. P. Wong, M. Lanza, *Nat. Electron.* **2018**, *1*, 458.
[4] D. Akinwande, C. Huyghebaert, C.-H. Wang, M. I. Serna, S. Goossens, L.-J. Li, H.-S. P. Wong, F. H. L. Koppens, *Nature* **2019**, *573*, 507.

© 2023 The Authors. Advanced Materials Interfaces published by Wiley-VCH GmbH

21967350, 2023, 7, Downloaded from https://onlinelibrary.wiley.com/doi/10.1002/admi.202202016 by EVIDENCE AID - BELGIUM, Wiley Online Library on [08/06/2023]. See the Terms and Conditions (https://onlinelibrary.wiley.com/terms-and-conditions) on Wiley Online Library for rules of use; OA articles are governed by the applicable Creative Commons License

[5] D. Akinwande, D. Kireev, *Nature* **2019**, *576*, 220.
[6] N. Flöry, P. Ma, Y. Salamin, A. Emboras, T. Taniguchi, K. Watanabe, J. Leuthold, L. Novotny, *Nat. Nanotechnol.* **2020**, *15*, 118.
[7] K. F. Mak, J. Shan, *Nat. Photonics* **2016**, *10*, 216.
[8] S. Das, J. A. Robinson, M. Dubey, H. Terrones, M. Terrones, *Annu. Rev. Mater. Res.* **2015**, *45*, 1.
[9] V. Kranthi Kumar, S. Dhar, T. H. Choudhury, S. A. Shivashankar, S. Raghavan, *Nanoscale* **2015**, *7*, 7802.
[10] H. Kim, D. Ovchinnikov, D. Deiana, D. Unuchek, A. Kis, *Nano Lett.* **2017**, *17*, 5056.
[11] Z. Cai, B. Liu, X. Zou, H.-M. Cheng, *Chem. Rev.* **2018**, *118*, 6091.
[12] X. Zhang, T. H. Choudhury, M. Chubarov, Y. Xiang, B. Jariwala, F. Zhang, N. Alem, G.-C. Wang, J. A. Robinson, J. M. Redwing, *Nano Lett.* **2018**, *18*, 1049.
[13] D. Chiappe, J. Ludwig, A. Leonhardt, S. El Kazzi, A. Nalin Mehta, T. Nuytten, U. Celano, S. Sutar, G. Pourtois, M. Caymax, K. Paredis, W. Vandervorst, D. Lin, S. De Gendt, K. Barla, C. Huyghebaert, I. Asselberghs, I. Radu, *Nanotechnology* **2018**, *29*, 425602.
[14] J. Mo, S. El Kazzi, W. Mortelmans, A. Nalin Mehta, S. Sergeant, Q. Smets, I. Asselberghs, C. Huyghebaert, *Nanotechnology* **2020**, *31*, 125604.
[15] Z. Zhang, P. Lin, Q. L. Liao, Z. Kang, H. N. Si, Y. Zhang, *Adv. Mater.* **2019**, *31*, 1806411.
[16] B. S. Liu, Q. L. Liao, X. K. Zhang, J. L. Du, Y. Ou, J. K. Xiao, Z. Kang, Z. Zhang, Y. Zhang, *ACS Nano* **2019**, *13*, 9057.
[17] L. Gao, Q. L. Liao, X. K. Zhang, X. Z. Liu, L. Gu, B. S. Liu, J. L. Du, Y. Ou, J. K. Xiao, Z. Kang, Z. Zhang, Y. Zhang, *Adv. Mater.* **2020**, *32*, 1906646.
[18] N. Kang, H. P. Paudel, M. N. Leuenberger, L. Tetard, S. I. Khondaker, *J. Phys. Chem. C* **2014**, *118*, 21258.
[19] G. López-Polín, C. Gómez-Navarro, V. Parente, F. Guinea, M. I. Katsnelson, F. Pérez-Murano, J. Gómez-Herrero, *Nat. Phys.* **2015**, *11*, 26.
[20] Y. T. Zhao, H. Y. Wang, H. Huang, Q. L. Xiao, Y. H. Xu, Z. N. Guo, H. H. Xie, J. D. Shao, Z. B. Sun, W. J. Han, X. F. Yu, P. H. Li, P. K. Chu, *Angew. Chem., Int. Ed.* **2016**, *55*, 5003.
[21] J. Shim, A. Oh, D. H. Kang, S. Oh, S. K. Jang, J. Jeon, M. H. Jeon, M. Kim, C. Choi, J. Lee, S. Lee, G. Y. Yeom, Y. J. Song, J.-H. Park, *Adv. Mater.* **2016**, *28*, 6985.
[22] L. Z. Zhuang, L. Ge, Y. S. Yang, M. R. Li, Y. Jia, X. D. Yao, Z. H. Zhu, *Adv. Mater.* **2017**, *29*, 1606793.
[23] X. M. Zheng, Y. H. Wei, J. X. Liu, S. T. Wang, J. Shi, H. Yang, G. Peng, C. Y. Deng, W. Luo, Y. Zhao, Y. Li, K. Sun, W. Wan, H. Xie, Y. Gao, X. Zhang, H. Huang, *Nanoscale* **2019**, *11*, 13469.
[24] Y. Shi, B. Groven, J. Serron, X. Wu, A. Nalin Mehta, A. Minj, S. Sergeant, H. Han, I. Asselberghs, D. Lin, S. Brems, C. Huyghebaert, P. Morin, I. Radu, M. Caymax, *ACS Nano* **2021**, *15*, 9482.
[25] W. Park, P. Juhun, J. Jingon, L. Hyungwoo, C. Kyungjune, H. Seunghun, L. Takhee, *Nanotechnology* **2013**, *24*, 095202.
[26] C. Durand, X. Zhang, J. Fowlkes, S. Najmaei, J. Lou, A.-P. Li, *J. Vac. Sci. Technol., B* **2015**, *33*, 02B110.
[27] Y. Han, Z. Wu, S. Xu, X. Chen, L. Wang, Y. Wang, W. Xiong, T. Han, W. Ye, J. Lin, Y. Cai, K. M. Ho, Y. He, D. Su, N. Wang, *Adv. Mater. Interfaces* **2015**, *2*, 1500064.
[28] M. Kubicek, G. Holzlechner, A. K. Opitz, S. Larisegger, H. Hutter, J. Fleig, *Appl. Surf. Sci.* **2014**, *289*, 407.
[29] H. Taghinejad, A. A. Eftekhar, P. M. Campbell, B. Beatty, M. Taghinejad, Y. Zhou, C. J. Perini, H. Moradinejad, W. E. Henderson, E. V. Woods, X. Zhang, P. Ajayan, E. J. Reed, E. M. Vogel, A. Adibi, *npj 2D Mater. Appl.* **2018**, *2*, 10.
[30] J. D. Cain, E. D. Hanson, V. P. Dravid, *J. Appl. Phys.* **2018**, *123*, 204304.
[31] A. Valsaraj, J. Chang, A. Rai, L. F. Register, S. K. Banerjee, *2D Mater.* **2015**, *2*, 045009.
[32] S. E. Panasci, E. Schilirò, G. Greco, M. Cannas, F. M. Gelardi, S. Agnello, F. Roccaforte, F. Giannazzo, *ACS Appl. Mater. Interfaces* **2021**, *13*, 31248.
[33] R. T. Eachambadi, H. T. S. Boschker, A. Franquet, V. Spampinato, S. Hidalgo-Martinez, R. Valcke, F. J. R. Meysman, J. V. Manca, *Anal. Chem.* **2021**, *93*, 7226.
[34] B. J. Tyler, G. Rayal, D. G. Castner, *Biomaterials* **2007**, *28*, 2412.
[35] B. Schuler, D. Y. Qiu, S. Refaely-Abramson, C. Kastl, C. T. Chen, S. Barja, R. J. Koch, D. F. Ogletree, S. Aloni, A. M. Schwartzberg, J. B. Neaton, S. G. Louie, A. Weber-Bargioni, *Phys. Rev. Lett.* **2019**, *123*, 076801.
[36] J. Lu, A. Carvalho, X. K. Chan, H. Liu, B. Liu, E. S. Tok, K. P. Loh, A. H. Castro Neto, C. H. Sow, *Nano Lett.* **2015**, *15*, 3524.
[37] S. Barja, S. Refaely-Abramson, B. Schuler, D. Y. Qiu, A. Pulkin, S. Wickenburg, H. Ryu, M. M. Ugeda, C. Kastl, C. Chen, C. Hwang, A. Schwartzberg, S. Aloni, S.-K. Mo, D. F. Ogletree, M. F. Crommie, O. V. Yazyev, S. G. Louie, J. B. Neaton, A. Weber-Bargioni, *Nat. Commun.* **2019**, *10*, 3382.
[38] A. Wu, Q. Song, H. Liu, *Comput. Theor. Chem.* **2020**, *1187*, 112906.
[39] Q. Liang, J. Gou, Arramel, Q. Z. , W. Zhang, A. T. S. Wee, *Nano Res.* **2020**, *13*, 3439.
[40] V. Spampinato, S. Armini, A. Franquet, T. Conard, P. van der Heide, W. Vandervorst, *Appl. Surf. Sci.* **2019**, *476*, 594.
[41] W. Mortelmans, S. E. Kazzi, A. N. Mehta, D. Vanhaeren, T. Conard, J. Meersschaut, T. Nuytten, S. D. Gendt, M. Heyns, C. Merckling, *Nanotechnology* **2019**, *30*, 465601.
[42] V. Spampinato, M. Dialameh, A. Franquet, C. Fleischmann, T. Conard, P. van der Heide, W. Vandervorst, *Anal. Chem.* **2020**, *92*, 11413.
[43] T. Hantschel, M. Tsigkourakos, L. Zha, T. Nuytten, K. Paredis, B. Majeed, W. Vandervorst, *Microelectron. Eng.* **2016**, *159*, 46.

© 2023 The Authors. Advanced Materials Interfaces published by Wiley-VCH GmbH

21967350, 2023, 7, Downloaded from https://onlinelibrary.wiley.com/doi/10.1002/admi.202202016 by EVIDENCE AID - BELGIUM, Wiley Online Library on [08/06/2023]. See the Terms and Conditions (https://onlinelibrary.wiley.com/terms-and-conditions) on Wiley Online Library for rules of use; OA articles are governed by the applicable Creative Commons License